Available Online

JSR Publications

J. Sci. Res. **15** (1), 141-157 (2023)

JOURNAL OF SCIENTIFIC RESEARCH

www.banglajol.info/index.php/JSR

Enhanced Anticarcinogenic and Antimicrobial Response of Synthesized Tungsten Oxide Nanoparticles

J. Kumari, P. Mangala*

Research Centre, Department of Chemistry, Jyoti Nivas College Autonomous, Bangalore University, Bangalore, Karnataka, India

Received 13 February 2022, accepted in final revised form 17 September 2022

Abstract

In the present study, we fabricated tungsten trioxide nanoparticles (WO_3 NPs) from a tungsten complex [$W(C_{13}H_{10}NO)_3$] of ligand *N*-salicylideneaniline with tungstic acid as the precursor. Nanoparticles were synthesized using the direct thermal decomposition method. These nanoparticles were evaluated for cytotoxicity influence on human breast cancer MCF7 cell line (adenocarcinoma). The observed results suggested that WO_3 can destroy 50 % of viable cells after 24 h of incubation at 37 °C. Based on these results, we concluded that WO_3 nanoparticles could be a potential drug carrier candidate against human breast cancer cells based on the amount of the drug. In addition, WO_3 nanoparticles exhibited significant antimicrobial and antifungal activity.

Keywords: Tungsten oxide nanoparticles; Biological activity; FT-IR; TGA; TEM.

doi: http://dx.doi.org/10.3329/jsr.v15i1.58211 J. Sci. Res. **15** (1), 141-157 (2023)

1. Introduction

In the last two decades, nanotechnology has emerged as the most promising area of scientific research and received considerable research attention. Nanotechnology refers to nano-sized (1–100 nm) particles and has been used in different fields. Although nanoparticles (NPs) have unique size-reliant properties [1,2], these cannot be considered a homogeneous family because of their highly varying chemical and physical properties; for example, carbon nanotubes, quantum dots (CdTe and CdSe) [3], liposomes, polymeric NPs [4], magnetic nanoparticles [5], micelles [6] as well as different kinds of metals (W, Au, Zn, etc.) and metal oxide nanoparticles. Metal oxide NPs are widely used in wastewater treatment, biosensing, gas sensing, catalysis, energy storage materials, automobile catalytic converters, and biomedical application [7]. WO_3 NPs are essential nano-sized materials that have been extensively used in biomedical and chemical fields. In addition, WO_3 NPs are widely known for their antibacterial efficiency toward gram-negative (*Escherichia coli*) and gram-positive (*Staphylococcus aureus*) bacteria. WO_3 NPs induce bacterial cell death via physical destruction, anti-biofilm effect, and oxidative

* *Corresponding author*: preetimangala@jyotinivas.org

stress mechanisms. The direct contact of WO_3 NPs with the bacterial cell surface resulted in the loss of cell membrane integrity, release of intracellular constituents, and cell death. In addition, we investigated the impact of biofilm formation against both strains [8]. Samaya *et al*. [9] reported WO_3^-deposited (40 mg/cm^2) and checked antibacterial activities against gram-positive, *Staphylococcus aureus*, and gram-negative *Klebsiella pneumoniae* bacteria. WO_3 NPs exhibited excellent antibacterial activities under both light illumination and dark conditions. In 2022, Manikandan *et al.* [10] studied fabricated the novel WO_3@g-C_3N_4@MWCNT nanohybrids and evaluated their photocatalytic antibacterial activity against *B. subtilis* and *K. pneumoniae*. Although they exhibited superior antibacterial activity against the gram-negative stain under light exposure, no effect was observed under dark. The gram-positive strain remained unaffected under both conditions. The highest photocatalytic antimicrobial activity could be attributed to the production of reactive oxygen species (ROS), followed by membrane disruption. In 2012, Srisitthiratkul *et al.* [11] studied fabricated nano silver decorated WO_3 nanofibers and evaluated their antibacterial activity against both *S. aureus* and *E. coli*. These nanofibers displayed prominent antibacterial activities against both strains.

In 2020, Chang *et al.* [12] reported synthesized composites of $W_{18}O_{49}$ nanorods and Ag/AgCl nanoparticles composed of the AgCl core and Ag shell and checked their antibacterial activities against *Vibrio natriegens*. Bacterial Ag/AgCl/$W_{18}O_{49}$ composites showed higher antibacterial activities, leading to the generation of high levels of ROS, which could destroy the bacterial cell wall and cause death in the same year (2020), Arshad *et al.* [13] investigated the fabricated Zn-doped-WO_3 NPs and evaluated their antibacterial efficacies toward several gram-negative and positive bacteria *(E. coli, Pasteurella multocida, B. subtilis,* and *S. aureus)*. The Zn-doped-WO_3 NPs exhibited superior antibacterial activities against all evaluated bacteria, which increased with an increasing amount of Zn doping. In 2020, Ozkazanc *et al.* studied composites of poly-N-methyl pyrrole (PNMPy) and WO_3 NPs and investigated their antibacterial activities toward *E. coli* and *S. aureus* strains [14]. The composites exhibited excellent antibacterial activities against both bacteria due to their interaction with the cell wall and subsequent membrane damage.

In addition to the antibacterial activity, WO_3 NPs possess excellent anticancer activity due to their profound ROS generation ability under light exposure. Being a semiconductor, WO_3 NPs undergo photoexcitation under light exposure and initiate electrons transfer from the valence band (VB) to the conduction band (CB), thereby generating electron-hole pairs. These photo-generated electrons reduce oxygen to superoxide radical ($O^{2\bullet-}$), whereas holes oxidize water to hydroxyl radicals (·OH). These reactive free radicals cause oxidative stress and lead to protein oxidation, mitochondrial disruption, and DNA denaturation, causing apoptosis of tumor cells [15-18]. However, doping with metals further increases their ROS generation efficacy by inhibiting the photo-generated electron-hole pair recombination, leading to increased anticancer potential. Furthermore, WO_3NPs show cancer cell-specific cytotoxicity under both light exposure and dark, whereas normal cells remain unaffected. Mehmood *et al*. [19-21]

studied the anticancer activities of Sn-, Ni-, and Co-doped WO_3 nanoplates (13, 25, and 48 nm, respectively) against human breast cancer (MCF-7) and liver carcinoma (HepG2) cells in the presence of LED light. In 2016, Selvamani *et al*. [22] studied the anticancer activities of $Ag@Ag8W_4O_{16}$ nano-roasted rice beads (length: 5–211 nm and breadth: 30–35 nm) against mice melanoma cell (B16F10) lines exposed to different concentrations (20–100 µg/mL) of $Ag@Ag_8W_4O_{16}$ for 24 h. $Ag@Ag_8W_4O_{16}$ observed dose-dependent cytotoxicity against skin cancer cells with an 82% reduction in cell viability at the highest concentration of 100 µg/mL. However, $Ag@Ag_8W_4O_{16}$ did not exhibit any significant cytotoxicity toward the human normal skin cell line (HaCaT) within the same concentration range, indicating their cancer cell-specific toxicity. Zhao *et al*. (2016) fabricated lanthanide-encapsulated nano-sized polyoxometalates $[H_2N(CH_3)_2]6Na_{24}H_{16}\{[Ln_{10}W_{16}(H_2O)_{30}O_{50}](B\text{-}\alpha\text{-}As\ W_9O_{33})_8\}\bullet 97H_2O$; Ln = Tb^{III}, Tm^{III}] and examined their anticancer activities against HeLa and MCF-7 cells. Nanocomposites have been reported to display enhanced cytotoxicity and apoptosis toward cancer cells as compared with mouse fibroblast (L929) cells [23-24]. In the same year, Wang *et al*. [25] reported the fabrication of composite gel from amorphous tungsten oxide (a-WO_3) and a polymer [poly (ethylene oxide)-block-poly (propylene oxide)-block-poly (ethylene oxide)]. They studied their anticancer activities using *in vitro* and *in vivo* working models. The localized electrons on a-WO_3 produced H_2O_2 under the exposure of the entire white light spectra via electron-hole separation. The H_2O_2 production was further increased upon UV irradiation at high temperatures. In addition, the localized electrons on a-WO_3 increased the absorption of the infrared light of the solar spectrum with a rapid increase in surface temperature. The composites triggered apoptosis in human skin cancer A375 cells by inducing oxidative stress, whereas no cytotoxicity was observed toward normal epithelial cells (NIH/3T3). Furthermore, they conducted an *in vivo* study using tumor-bearing mice that were topically treated with the composite gel. The tumor volume of treated mice was significantly decreased following laser irradiation via synergistic photodynamic and photothermal therapy. In 2018, Jeevitha *et al*. [26] investigated the dose-dependent anticancer potential of graphene oxide (GO)-WO_3 nanocomposites and found that (<150 nm) in human lung cancer (A-549) cells treated with different concentrations (31.2–250 µg/mL) of GO-WO_3 nanocomposites for 24 h, GO-WO_3 nanocomposites exhibited a higher anticancer activity with an IC_{50} value of 139.6 µg/mL than bare WO_3 with an IC_{50} value of 255.7 µg/mL.

Most of the tungsten oxide nanoparticles are synthesized by precipitation and using hydrothermal/solvothermal methods because of their easiness and large-scale production. However, these techniques sometimes involve the use of toxic organic solvents and produce side products. Therefore, WO_3 NPs have been used to analyze the antimicrobial activity of tungsten oxide NPs. Our study comprises the synthesis of pure tungsten oxides from their respective metal complexes using the direct thermal decomposition method. Here we synthesized *N*-salicylideneaniline and characterized it by ^{1}H NMR and ^{13}C NMR. Metal oxide NPs were synthesized from their respective complexes, and their biomedical applications, such as antibacterial, antifungal, and anticancer activities, were studied.

2. Experimental

2.1. *Materials and reagents*

Salicylaldehyde was purchased from Sigma Aldrich, India, with 99 % purity. Aniline was purchased from Merck India, with a 99 % purity index, and tungstic acid (H_2WO_4) was procured from Sigma Aldrich. *N*-salicyclideneaniline, methanol, and ethanol were purchased from Sigma Aldrich, India, with 99 % purity. Ethyl acetate was purchased from Sigma Aldrich, India, with 99 % purity.

2.2. *Apparatus*

The NMR spectra were recorded at the Bruker NMR Research Centre, IISc, Bengaluru, using the modulation EXT40218 spectrometer (USA) using dimethyl sulfoxide (d_6) solvent. The synthesized tungsten complex [W $(C_{13}H_{10}NO)_3$] and WO_3 NPs were analyzed using the Rigaku Smartlab X-ray diffractometer, Centre for Nano Science and Engineering (CeNSE), IISc, Bengaluru, (Japan) TGA-DTA was recorded on Perkin Elmer STA 8000, (USA) UV-Visible and FT-IR spectra were obtained using the Shimadzu spectrophotometer, CeNSE, IISc, Bengaluru (Model MPC-3100), USA and FT-IR Perkin Elmer spectrophotometer, respectively. SEM EDX analysis by Zeiss Gemini Instrument and EDX Bucker, CeNSE, IISc, Bengaluru, modulation CAL4231 (USA), and TEM analysis by Instrument FEI-Titan Themis 300 KV CeNSE, IISc, Bengaluru, USA, was conducted for tungsten oxide NPs.

2.3. *Preparation of ligand N-salicylideneaniline ($C_{13}H_{11}NO$)*

To prepare the ligand, salicylaldehyde (1.22 g, 10 mmol) in methanol (10 mL) was added dropwise to a solution of aniline (1.22 g, 13.7 mmol) in methanol (10 mL). The solution was stirred at room temperature (27 °C) for 5 h. Next, the solvent was allowed to evaporate, and the obtained yellow color precipitate was filtered and dried. Thin-layer chromatography (TLC) was used to monitor the progress. The crude product was recrystallized with ethyl acetate (yield: 2.08 g) [27].

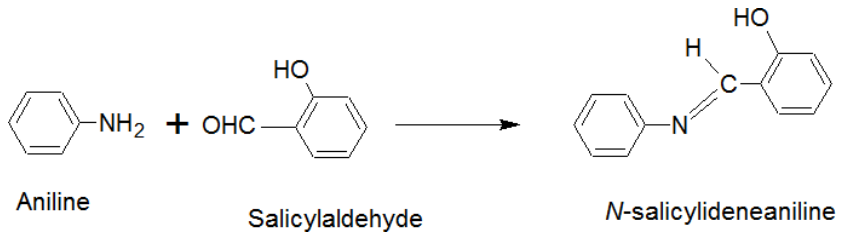

Scheme 1. Preparation of *N*-salicylideneaniline.

2.4. *Preparation of WO_3 NPs*

WO_3 NPs were synthesized from tri-*N*-salicylideneaniline tungsten [$W(C_{13}H_{10}NO)_3$], which was used as a precursor. Next, 0.5 g of tungstic acid (H_2WO_4) and 2.0 g of *N*-salicylideneaniline ($C_{13}H_{11}NO$) were added to ethanol (30 mL), and the reaction was allowed to run for 5 h with continuous stirring at 40 °C. The complex mixture formed was kept for drying at room temperature for 2 days. The yield of the complex was 2.075 g. The complex was placed in a muffle furnace at 600 °C for 4 h and weighed again. The final yield of the product obtained after calcination was 0.547 g.

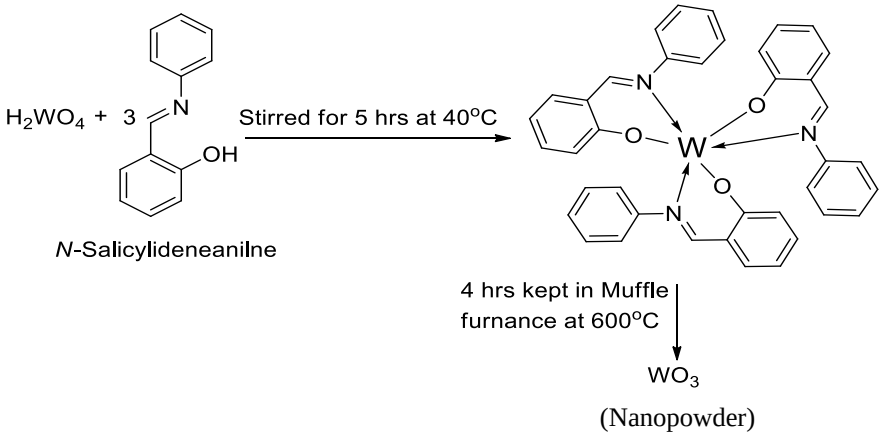

Scheme 2. Synthesis of tungsten complex with *N*-salicylideneaniline and further by calcination of complex and formation of WO_3 NPs.

2.5. *Determination of anticancer activity and antimicrobial activity*

Cell lines MCF7-human breast adenocarcinoma cell line (NCCS, Pune), cell culture medium: DMEM high-glucose media (#AT111, HiMedia), adjustable multichannel pipettes and a pipettor (Benchtop, USA), fetal bovine serum (#RM10432, HiMedia), MTT reagent (5 mg/mL) (# 4060 HiMedia), dimethyl sulfoxide (#PHR1309, Sigma), camptothecin (#C9911, Sigma), D-PBS (#TL1006, HiMedia), 96-well plate for culturing the cells (Corning, USA), T25 flask (# 12556009, BioLite-Thermo), 50 mL centrifuge tubes (# 546043 Tarson), 1.5 mL centrifuge tubes (Tarson), 10 mL serological pipettes (Tarson), 10 to 1000 µL tips (Tarson), *in vitro* antibacterial activities were examined for the given sample (bulk and NPs) [28]. Antibacterial activities of samples were studied using the agar diffusion method. The samples were used to determine the zone of inhibition or sensitivity against *E. coli*, *S. aureus*, *Bacillus* sp, and *Pseudomonas* sp strains. Antifungal activities of samples were investigated, and samples were used to determine the zone of inhibition or sensitivity against *Aspergillus* sp and *Trichoderma* sp.

2.5.1. *Cell line and cell culture of anticancer activity experiment*

A seed of 200 µg cell suspension was used without the test agent in a 96-well plate at essential cell density (20,000 cells per well). Cells were grown to an appropriate concentration, and the plate was incubated for 24 h at 37 °C in a 5 % CO_2 atmosphere. The plate was taken out from the incubator after the incubation period, and the spent media were discarded. The MTT reagent was added to a final concentration of 0.5 mg/mL of the entire volume. A wrapped plate with aluminum foil was used to avoid exposure to light. The plate was returned to the incubator for 3 h, following which the MTT reagent was removed, and subsequently, 100 µg of the solubilization solution (dimethyl sulfoxide) was added. It was gently stirred in a gyratory shaker to enhance dissolution. Occasionally, pipetting up and down was done to completely dissolve the MTT formazan crystals, especially in dense cultures.

2.5.2. *Cell viability assay*

The MTT assay was used to determine the effect of WO_3 nanoparticles on cell viability. In short, cells (3×10^4 cells/mL) were seeded in 96-well plates in 200 µg of a medium comprising antibiotics and 10 % FBS. After 24 h, cells were treated with different concentrations of WO_3. After 48 h, 20 µg of the MTT solution was added to each well, followed by incubation in a humidified environment for 4 h. Afterward, the supernatant was removed, and 150 µg of dimethyl sulfoxide was added. For 30 min, plates were shaken in the dark, and subsequently, a sunrise microplate reader was used to measure the absorbance at 570 nm. The viability of cells is depicted as a percentage of the control viability (mean ±SD). The blank contained 200 of RPMI 1640 or DMEM-F12 with 10 % FBS and equivalent reagent concentrations. All experiments were conducted in triplicate.

2.5.3. *Antibacterial activity*

The antibacterial activities were studied using the agar diffusion method [29]. The nutrient agar was prepared as per the following composition: peptones 0.5 % (concentration), yeast extract 0.3 %, sodium chloride 0.5 %, agar 1.5 %, pH 5.6 ±0.2, distilled water 1000 mL. These were autoclaved at 121 °C and 15 lbs. and cooled and poured onto sterilized Petri plates, allowing solidification. Samples were poured into different plates after solidification, and plates were incubated at 37 °C for 24 h. Bulk molybdenum trioxide was used as a standard compound for comparison. The antibacterial activity was dependent on the zone of inhibition in mm; if the inhibition zone was < 7 mm, the sample showed less antibacterial activity. If the inhibition zone was > 7 mm, the sample showed better antibacterial activity. Considering the above-mentioned points, the metal NP screening for antimicrobial activity was performed.

2.5.4. *Antifungal activity*

The antifungal activities of samples were investigated using the agar diffusion method. The zone of inhibition or sensitivity against *Aspergillus* sp. and *Trichoderma* sp. was determined. The antifungal activities were studied using potato dextrose/Sabouraud dextrose agar medium. The agar medium was prepared as per the composition of dextrose (glucose), 40 g (concentration g/L), peptone 10 g (concentration g/L), agar 15 g (concentration g/L), pH 5.6 ±0.2, distilled water 1000 mL autoclaved at 121 °C or 15 lbs and cooled before being poured onto sterilized Petri plates and allowed for solidification. The wells were made after the solidification, and the samples were poured into different plates, which were incubated at 26 to 28 °C for 48 to 72 h. The incubated plates were observed for antifungal activities (zones of diameter were observed).

3. Results and Discussion

The synthesized ligand was checked by NMR spectra recorded in the Bruker EXT 40218 spectrometer using dimethyl sulfoxide (d_6) solvent at 25 °C. In the ^{1}H NMR, the presence of nine aromatic protons, one hydroxyl proton (δ 8.94), and one imine proton (δ 13.13) indicated the formation of the new compound. This was further supported by its ^{13}C NMR spectrum, where a signal at δ 163.9 indicated the presence of an imine group in the molecule. Furthermore, the signal at δ 148.5 was attributed to the carbon of ring (B) attached to the nitrogen. Other aromatic carbon signals appeared at δ 117.1–133.2. Thus, the ligand was assigned as N-salicylideneaniline ($C_{13}H_{11}NO$) [30]. ^{1}H NMR (400 MHz, DMSO-d_6): δ_H 6.98–6.99 (d, J = 7.2 Hz, 2H), 7.31–7.39 (d, J = 7.2 Hz, 1H), 7.31–7.46 (m, 5H), 7.65–7.70 (t, J = 7.2 Hz, 1H), 8.94–8.95 (t, J = 7.2 Hz, 1H), 13.13 (s, 1H); ^{13}C NMR (100 MHz, DMSO-d_6): δ_C 163.9, 160.0, 148.5, 133.2, 132.0, 129.0, 127.0, 121.0, 119.0, 117.1.

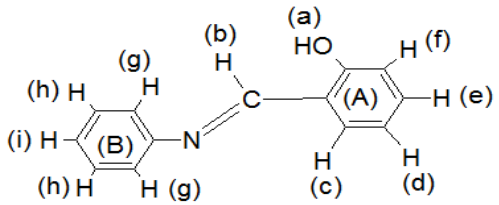

Scheme 3. Structure of *N*-salicylideneaniline (ligand).

3.1. *UV-Visible and FT-IR spectra of tungsten complex/capping solution*

Fig. 1(a) shows the absorption spectra of the tungsten complex [$W(C_{13}H_{10}NO)_3$] determined by UV–visible spectroscopy. The capping solution ligands stabilize the interface where nanoparticles interact with their medium of preparation. Specific structural features of nanoparticles are attributed to capping on their surfaces. These stabilizing agents play a key role in altering biological activities. The UV–visible spectra

of the complex exhibit visible transition due to the metal-ligand complex. The electronic absorption spectra of the tungsten complex consisted of a strong band at 327 nm (with quinoline ligand, Youssef *et al*.) [31]. In the tungsten complex, the observed strong band at 307 nm (*N*-salicylideneaniline ligand). This band was slightly affected by the polarity of the solution, corresponding to π-π* transitions. Sometimes, a redshift of this band was observed for the tungsten complex in benzene derivative with a wide spectrum.

Fig. 1(b) shows FT-IR spectra of the tungsten complex. The infrared spectrum provides information regarding the nature of the functional group attached to the metal atom. In this complex, the FTIR spectra of the tungsten complex, the band at 1616 cm^{-1} represents W =N stretching, and the band at 1582 cm^{-1} is due to C =N stretching vibration. The band at 1562 cm^{-1} may be associated with benzene ring stretching of C =C. There was no peak corresponding to an unreacted primary amine. The appearance of broadband at 3999 cm^{-1} corresponded to tungsten-oxygen stretching. The band at 1274 cm^{-1} indicates that the free nitrate group is present in the complex. The appearance of the band in the IR spectra of the complex at 1492 cm^{-1} and the band in the range of the peak at 445 cm^{-1} belongs to W–N–W stretching vibrations, the peaks at 521 and 692 cm^{-1} belong to the O-W-O stretching in the complex. The tungsten complex W-O-W bond appeared around 767 and 843 cm^{-1}. The stretching vibration of the W–O–W linkage gives rise to a characteristic intense band peaking at 692 cm^{-1} [32]. Tungsten-nitrogen multiple bonds are stretching modes with bands at 1068 cm^{-1} and 1084 cm^{-1} in the IR spectra.

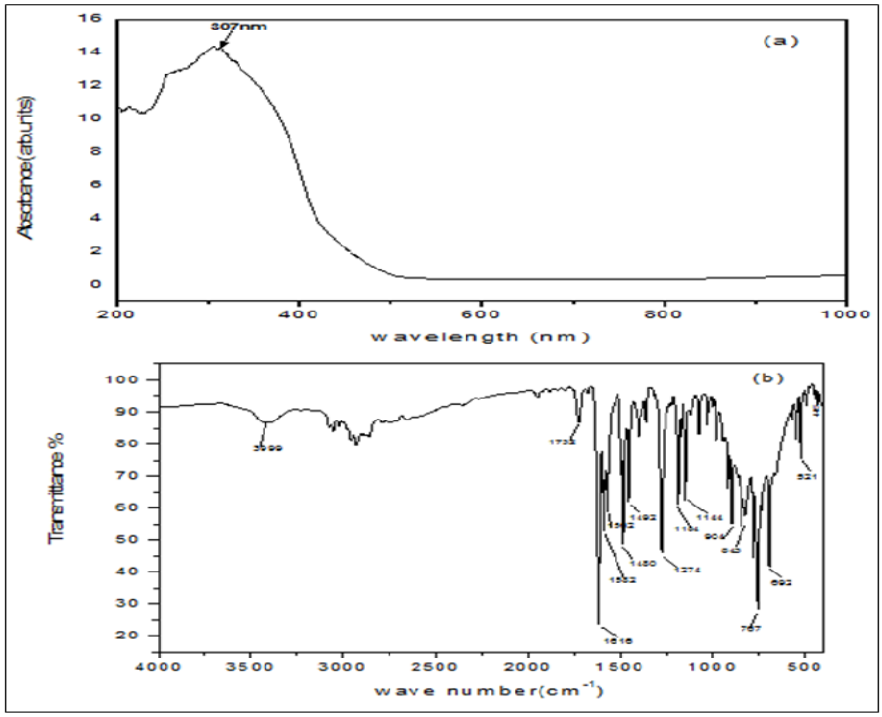

Fig. 1. (a) UV–visible spectra of the tungsten complex with *N*-salicylideneaniline as the ligand, (b) FT-IR spectra of the tungsten complex with *N*-salicylideneaniline as the ligand.

3.2. *TGA-DTA analysis of tungsten complex with N-salicylideneaniline [$W(C_{13}H_{10}NO)_3$] as ligand*

The thermal stability of the tungsten complex was studied at a temperature range of 40 °C to 900 °C at a heating rate of 10 °C per min. The thermogram, TG-DTA of the tungsten complex, is depicted in Fig. 2. The TG curve showed that the decomposition occurred at 245 °C. The first step involved the loss of coordinated water molecules in the temperature range of 192–245 °C for tungsten complexes. The first stage of decomposition occurred, indicating a weight loss of 34 % [33]. The thermal decomposition occurs between 192 °C and 245 °C. After 190 °C, a gradual weight loss was observed due to the decomposition of the metal-ligand bond of the prepared sample. However, thermal effects were observed in the DTA curve, showing the endothermic peak at 190 °C, which was due to the melting of the tungsten complex. However, after 245 °C, the complex was stable up to 800 °C without further decomposition of the complex.

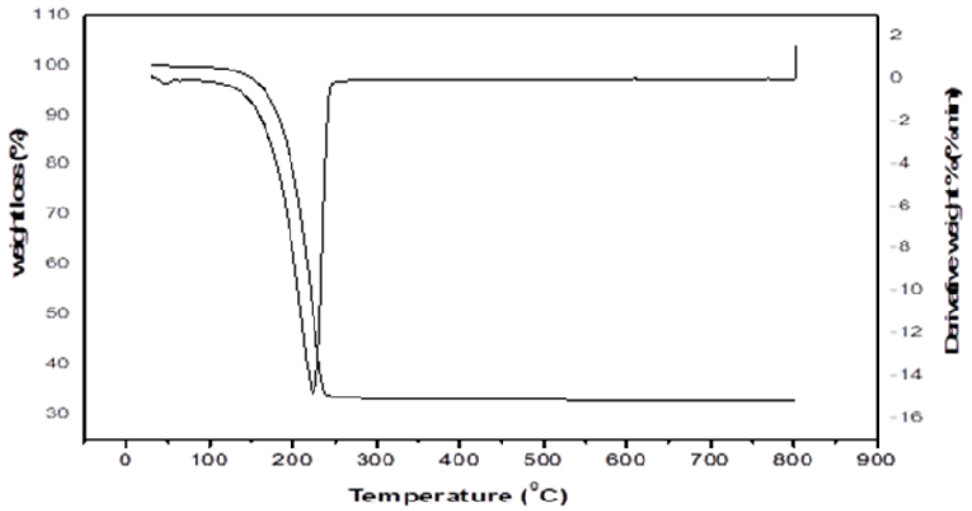

Fig. 2. TGA-DTA of the tungsten complex with *N*-salicylideneaniline as the ligand.

3.3. *UV–Visible and FT-IR spectra of synthesized WO_3 NPs*

The WO_3 shows an absorption edge at around 339 nm in Fig. 3a. The absorption spectrum was further analyzed by plotting $(\alpha hv)^2$ against hv or energy based on equation 1.

$$(\alpha hv)^2 = A(hv-Eg)^n \quad (1)$$

where α is the absorption coefficient, A is a constant independent from frequency v, n is the exponent that depends upon the quantum selection rules for the particular materials, and Eg is the band gap of the material. This relationship gives Eg by extrapolating the straight portion of $(\alpha hv)^2$ against the hv plot shown in Fig. 3b. Synthesized WO_3 NPs display a band gap energy of approximately 2.9 eV. This result is in agreement with other

studies reporting a band gap for monocline crystalline WO_3 NPs of approximately, having a high absorption in both UV and visible regions. This implies that these compounds show great photocatalytic activity under visible light because WO_3 NPs have a relatively small band group (2.6 eV to approx. 3.1 eV). It has photocatalytic activity in the visible region [34].

The FT-IR spectrum of WO_3 NPs (Fig. 3c) shows strong absorptions at 775 and 845 cm^{-1} associated with W-O-W stretching modes. The weak bands at 1280, 1470, and 1730 cm^{-1} are assigned to the stretching of W =O bonds at the surface. In addition, 2938 cm^{-1} corresponds to tungsten-oxygen stretching and bending modes of the lattice [35,36].

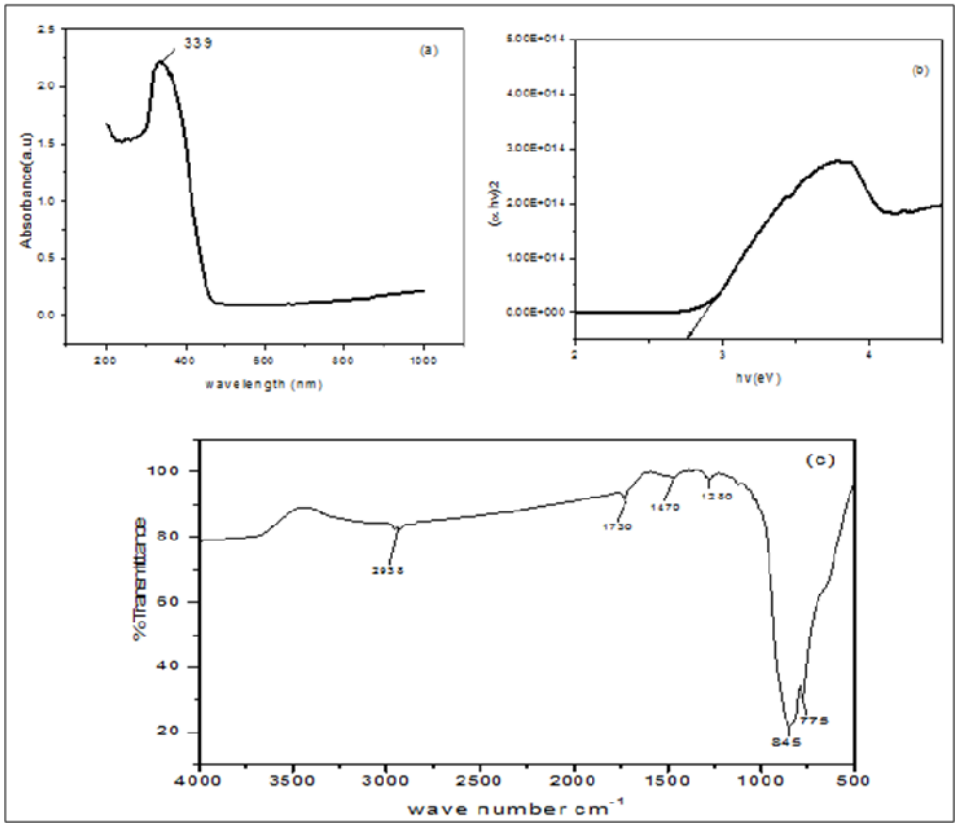

Fig. 3. (a) UV–visible absorption spectrum of WO_3 NPs. (b) Band gap spectrum of WO_3 NPs. (c) FT-IR spectrum of WO_3 NPs.

3.4. *PXRD analysis of WO_3 NPs*

The XRD analysis of WO_3 NPs was performed using the Rigaku Smart Lab X-ray diffractometer. Fig. 4 represents the XRD pattern of WO_3 powder. The wavelength used for XRD analysis is Cuk_α 1.540 (**Å**). The peaks corresponding to (011), (111), (002), (020), (200), (012), (202), (114), and (420) were due to the monoclinic crystal structure of

WO_3. We noted that all XRD peaks matched the standard. JCPDS No: No: 01–083–0950 as WO_3 NPs. From XRD data, the crystallite size (D) of prepared WO_3 NPs was 45 nm. Using the Debye–Scherrer equation: $D = k\lambda/d \cos\theta$, where d is the full width at half maximum or half-width in radians, k is the crystallite shape factor, which usually takes a value of about 0.9, and λ is the wavelength of X-ray source used in XRD [37].

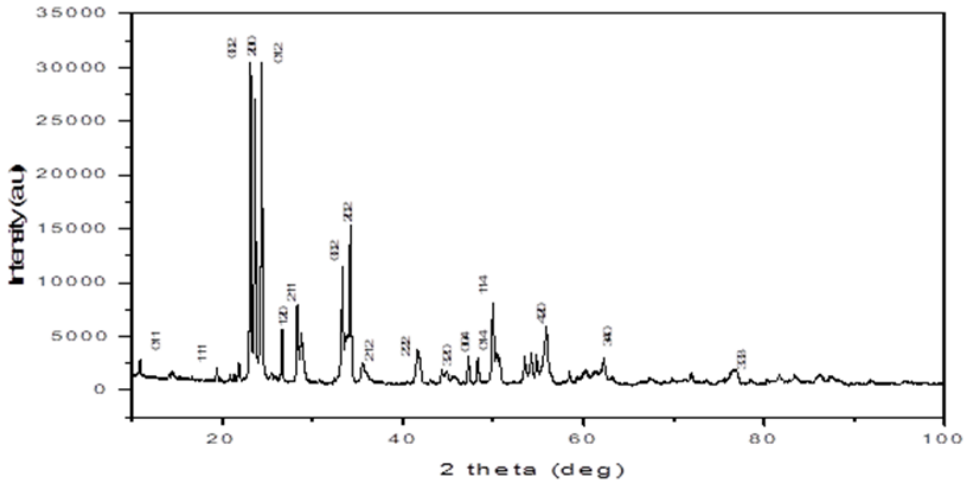

Fig. 4. PXRD pattern of WO_3 NPs.

3.5. *TGA-DTA analysis of WO_3 NPs*

To understand the thermal stability and relative weight loss of the material, thermogravimetric and differential thermal analyses were conducted. The analyses were performed under a nitrogen atmosphere of 20 $cm^3\ m^{-1}$ at a rate of 10 min^{-1}. The TGA and DTA curves of WO_3 NPs are shown in Fig. 5. The WO_3 NPs show excellent thermal stability up to 800 °C with negligible weight loss of around 0.7% due to a baseline drift of TGA, without any stage of decomposition. Hence, the results showed that WO_3 NPs exhibited a higher flame resistance and thermal stability [38-41].

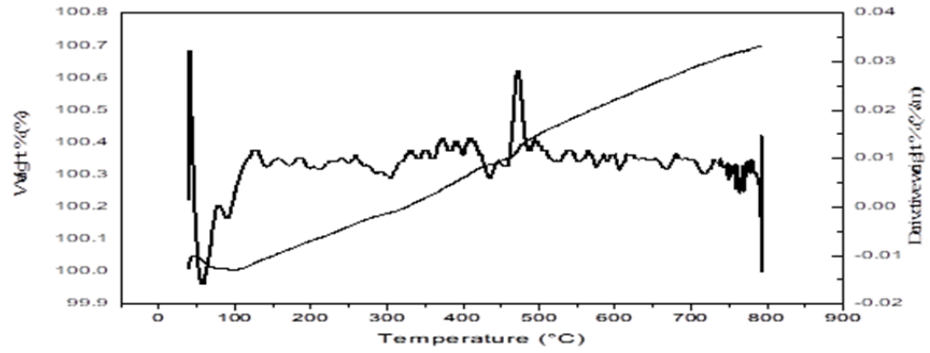

Fig. 5. TGA-DTA curves of WO_3 NPs.

3.6. *SEM and EDX of WO_3 NPs*

The SEM images of the WO_3 NPs triclinic crystal structure are shown in Fig. 6. The majority of the particles are approximately spherical in shape and size, ranging from 40 to 60 nm. The images showed that the particles are smaller in size. EDX spectroscopy analysis was performed to verify the chemical composition of the material. Fig. 7 shows the EDX spectra of WO_3 NPs, showing that the surface of WO_3 NPs exhibited elements of W and O [42-43].

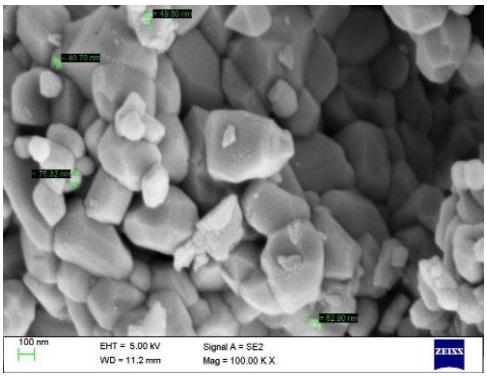

Fig. 6. SEM image of WO_3 NPs.

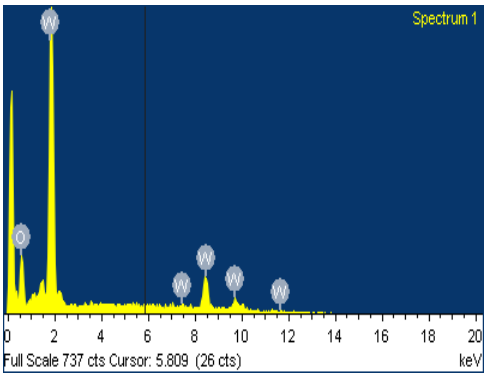

Fig. 7. EDX spectrum of WO_3 NPs.

3.7. *TEM image of WO_3 NPs*

TEM microscopy was performed to cross-identify the particle size of synthesized WO_3 powder. The prepared WO_3 powder is shown in Fig. 8a. The obtained particle-like structure was observed in the prepared sample of WO_3 NPs, which have an average particle size of 40 to 60 nm. The CBED pattern is shown in Fig. 8b, which provides information about the crystallinity of the prepared sample. The WO_3 powder was perfectly crystalline in nature and on nanoscale [43].

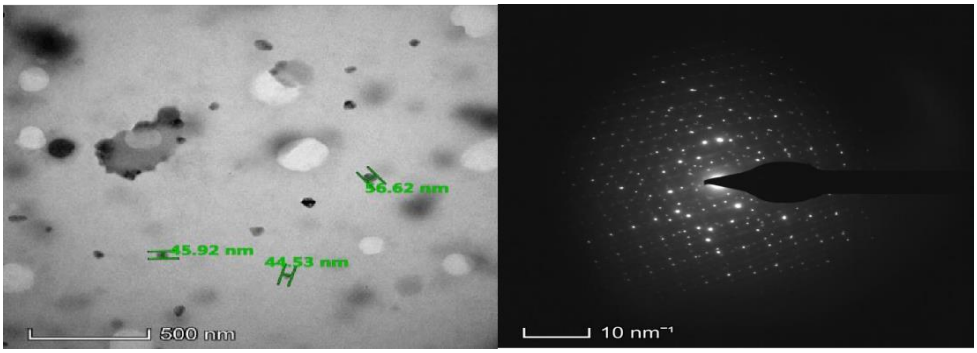

Fig. 8 (a) TEM image of WO_3 NPs, (b) TEM CBED pattern of WO_3 NPs.

4. Anticancer Activity

The cytotoxic profile of WO_3 powder (bulk/NPs) was examined against human breast cancer cell line MCF7 using the MTT assay is shown in Figs. 9 and 10. Two tested compounds were evaluated to check the cytotoxicity activity toward MCF-7. The used concentrations of the compound to treat the cells are shown in Table 1 [44].

Table 1. Drug treatment at different concentrations.

SI. No	Test compounds	Cell line	Concentration treated to cells
1	Untreated	MCF7	No treatment
2	Standard (camptothecin)	MCF7	10 µg/mL
3	Blank	–	Only Media without cells
4	Bulk WO_3	MCF7	12.5, 25, 50, 100, 200 µg/mL
5	Nanoparticles of WO_3 (NPs)	MCF7	12.5, 25, 50, 100, 200 µg/mL

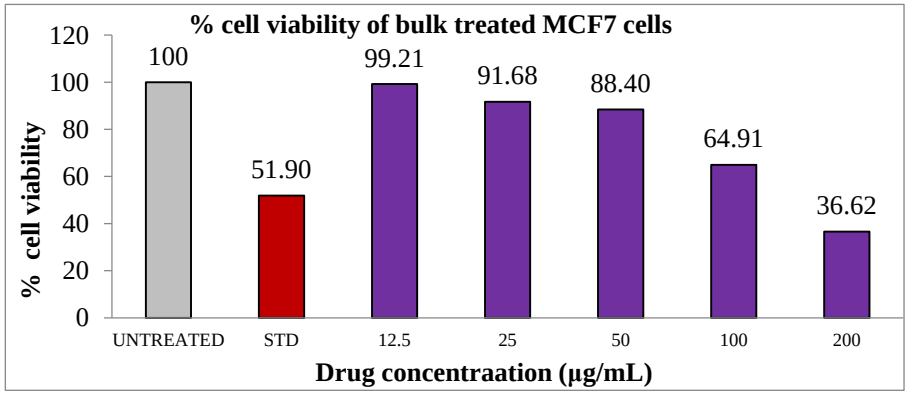

Fig. 9. Cell viability of bulk WO_3 NPs-treated MCF7 cells with different concentrations in comparison to the control.

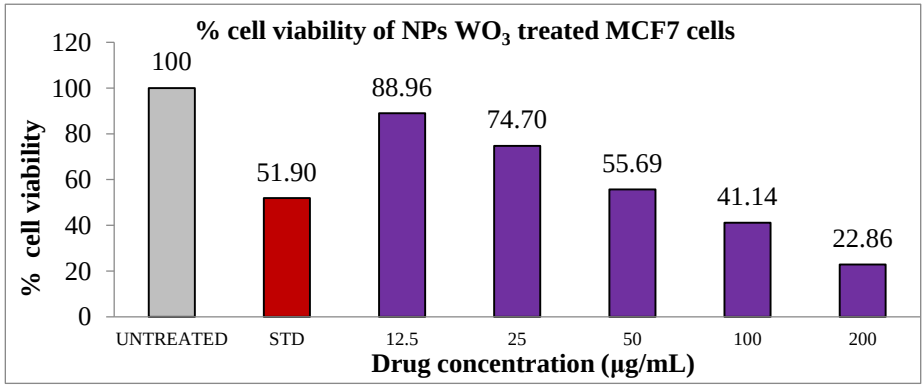

Fig. 10. Cell viability of WO_3 NPs-treated MCF7 cells with different concentrations in comparison to the control.

Table 2. IC_{50} concentration of bulk WO_3 and NPs WO_3 against MCF7 cells.

Sl. No	Sample code	IC_{50} (µg/mL)
1	Bulk WO_3	155.85
2	NPs WO_3	66.18

The bulk of WO_3 and NPs WO_3 NPs showed potential cytotoxic properties with IC_{50} concentrations of 155.85 µg/mL and 66.18 µg/mL is shown in Table 2, compared to the standard drug, i.e., camptothecin at a concentration of 10 µg/mL, by MTT cytotoxicity study by the ELISA reader. The results indicated that WO_3 NPs exerted a significant anticancer effect against human breast cancer cells due to their IC_{50} value.

4.1. *Antimicrobial activity*

The antimicrobial activity of bulk and NPs-WO_3 was investigated against *E. coli* and *S. aureus*, *Bacillus sp*, and *Pseudomonas sp* using the agar well-diffusion assay method. The inhibition zones (mm) around each well contained NPs and bulk WO_3. Among the tested bacteria, the NPs samples were loaded on pre-inoculated plates of bacterial strains with various concentrations ranging from 100 to 400 µL. The NPs were the most resistant, with a minimum inhibition zone of 2 mm for *S. aureus* at 200 µL/mL concentration. The same NPs showed a 2 mm minimum zone of inhibition at 300 µL/mL concentration; however, at 400 µL/mL concentration, *E. coli* exhibited the maximum zone of inhibition of around 8 mm, showing a better antimicrobial potential. *Bacillus sp.* and *Pseudomonas* sp. were checked for antibacterial activity against NPs are shown in Table 3. The concentration of 200 µL/mL for *Bacillus* sp. showed a maximum inhibition zone of around 4 mm, whereas a 2 mm zone of inhibition was found against *Pseudomonas* sp. The concentration of NPs was 200 µL/mL.

In addition, bulk samples at different concentrations showed no zone of inhibition at 100, 200, and even 300 µL/mL are shown in Table 4. It showed extremely poor efficiency of a bulk sample against NPs of tungsten oxide. The bulk sample showed a resistant zone of inhibition at 400 µL/mL and showed a 2 mm zone of inhibition for *S. aureus*. In the bulk sample, 400 µL/mL showed a better zone of inhibition, and for *E. coli*, around a 5 mm zone of inhibition was observed. *Bacillus* sp. showed a 6 mm zone of inhibition at 400 µL concentration. Even *Pseudomonas* sp. showed a positive minimum resistant zone of inhibition of 1 mm.

Hence, WO_3 NPs showed enhanced antibacterial activity against bulk samples and could cause morphological alterations in the bacterial cell wall. The mechanism of action of the antibacterial activity of WO_3 NPs could involve targeting the respiratory chain and cell division, ultimately leading to cell death.

Table 3. *In vitro* antibacterial screening of synthesized WO_3 NPs.

Sample	Concentration in µL	*S. aureus*	*E. coli*	*Bacillus* sp.	*Pseudomonas* sp.
		Diameter of zone of inhibition in mm			
NPs	25 µg/mL (100 µL/mL)	0	0	0	0
	25 µg/mL (200 µL/mL)	2	0	0	0
	25 µg/mL (300 µL/mL)	4	2	4	5
	25 µg/mL (400 µL/mL)	3	8	5	3

Table 4. *In vitro* antibacterial screening of synthesized bulk WO_3.

Sample	Concentration in µL	*S. aureus*	*E. coli*	*Bacillus* sp.	*Pseudomonas* sp.
		Diameter of zone of inhibition in mm			
bulk	25 µg/mL (100 µL/mL)	0	0	0	0
	25 µg/mL (200 µL/mL)	0	0	0	0
	25 µg/mL (300 µL/mL)	0	0	0	0
	25 µg/mL (400 µL/mL)	2	5	6	1

4.2. *Antifungal activity*

The antifungal activity of bulk and NPs samples against *Aspergillus* sp. and *Trichoderma sp* was recorded. At 100 µL/mL concentration, NPs showed a 1 mm minimum zone of inhibition for *Aspergillus sp*, and in the case of *Trichoderma sp*, no zone of inhibition was observed. NPs were susceptible at that concentration. A concentration of 200 µL/mL NPs showed a maximum 3 mm zone of inhibition for *Aspergillus* sp. and *Trichoderma* sp. Hence, the sample NPs were found to have potent antifungal activity. The bulk sample showed a 1 mm zone of inhibition for *Aspergillus sp* at 100 µL/mL, whereas no zone of inhibition was observed for *Trichoderma* sp. at 100 µL/mL. *Aspergillus* sp. showed a 2 mm elevated zone of inhibition for 200 µL/mL. A 1 mm zone of inhibition was observed in the case of *Trichoderma* sp. Hence, we studied the antifungal activity of WO_3 NPs and bulk sample WO_3 against *Aspergillus* sp. and *Trichoderma* sp.

5. Conclusion

The objective to synthesize tungsten trioxide nanoparticles (WO_3 NPs) from tungsten complex of *N*-salicylideneaniline, $[W(C_{13}H_{10}NO)_3]$, was achieved successfully. In the current study, WO_3 NPs were successfully synthesized from a tungsten complex using *N*-salicylideneaniline $[W(C_{13}H_{10}NO)_3]$ as the ligand. The ligand plays a significant role in controlling the segregation of the particle size. The SEM microstructure indicated the formation of spherical nanoparticles in the range of 40 to 60 nm. The TGA analysis revealed the stability of synthesized compounds at a higher temperature (800 °C). Bulk WO_3 and WO_3 NPs showed an IC_{50} concentration against MCF7 cells at 155.85 µg/mL and 66.18 µg/mL, respectively, following 24 h of incubation at 37 °C. The observations strongly suggested that the tested compound, namely, WO_3 NPs, could have possible therapeutic potential against human breast cancer cells based on the dosage of the drug.

Furthermore, the compound WO_3 NPs showed excellent antibacterial activity and antifungal activity and can be used as a promising antibacterial agent in wide applications.

Acknowledgments

Sincere thanks to Sr. L. Thomas and Management of Jyoti Nivas College Autonomous and Research Centre, Department of Chemistry, Jyoti Nivas College Autonomous, Bangalore for extending their support and providing infrastructure to carry out the research work. We are thankful to the Sophisticated Instrumentation Facility (SIF), School of Advanced Sciences Chemistry Division, Vellore Institute of Technology (VIT), Vellore, the Department of Inorganic and Physical Chemistry, Centre for Nano Science and Engineering (CENSE), Indian Institute of Science (IISc), and the Scientific and Industrial Research Center, Bengaluru. We extend our gratitude to Department of Studies in Chemistry, Bangalore University.

References

1. S. Cong, F. Geng, and Z. Zhao, Adv. Mater. **28**, 47 (2016). https://doi.org/10.1002/adma.201601109
2. F. Malara, A. Cannavale, S. Carallo, and G. Gigli, ACS Appl. Mater. Interfaces **6**, 12, 9290 (2019). https://doi.org/10.1021/am501648z
3. C. G. Granqvist, Thin Solid Films **564**, 1 (2014). https://doi.org/10.1016/j.tsf.2014.02.002
4. H. Zheng, Y. Tachibana, and K. Kalantar-Zadeh, Langmuir **26**, 24 (2010). https://doi.org/10.1021/la103692y
5. A. Marikutsa, L. Yang, M. Rumyantseva, M. Batuk, J. Hadermann, and A. Gaskov, Sensors Actuators B: Chem. **277**, 336 (2018). https://doi.org/10.1016/j.snb.2018.09.004
6. L. Hu, P. Hu, Y. Chen, Z. Lin, and C. Qiu, Front. Chem. **6**, 452 (2018).
7. H. Zhang, W. Chen, and H. Zhang, J. Nanoelectron. Optoelectron. **13**, 1141 (2018). https://doi.org/10.1166/jno.2018.2382
8. W. Yaipimai, N. Subjalearndee, G. Tumcharern, and V. Intasanta, J. Mater. Sci. **50**, 7681 (2015). https://doi.org/10.1007/s10853–015–9333–1
9. U. Baig, M. A. Gondal, S. Rehman, and S. Akhtar, Appl. Nanosci. **10**, 851 (2020). https://doi.org/10.1007/s13204–019–01186-z
10. V. S. Manikandan, S. Harish, J. Archana, and M. Navaneethan, Chemosphere **287**, 132050 (2022). https://doi.org/10.1016/j.chemosphere.2021.132050
11. P. S. Saud, B. P. Saud, A. P. Tiwari, Z. K. Ghouri, M. Park, and H. K. Kim, J. Colloid Interface Sci. **465**, 225 (2016). https://doi.org/10.1016/j.jcis.2015.11.072
12. X. Chang, S. Sun, L. Dong, and Y. Yin, Mater. Lett. **83**, 133 (2012) https://doi.org/10.1016/j.matlet.2012.06.018
13. M. Arshad, S. E. Haque, M. Bilal, N. Ahmad, A. Ahmad, M. Abbas, J. Nisar, M. I. Khan, A. Nazir, A. Ghaffar, and M. Iqbal, Mater. Res. Express **7**, 15407 (2020). https://doi.org/10.1088/2053–1591/ab6380
14. G. Duan, L. Chen, Z. Jing, P. D. Luna, L. Wen , L. Zhang, L. Zhao, J. Xu , Zhen Li , Z. Yang, and R. Zhou, Chem. Res. Toxicol. **32**, 1357 (2019). https://doi.org/10.1021/acs.chemrestox.8b00399
15. C. Castillo, G. Cabello, B. Chornik, Y. Huentupil, and G.E. Buono-Core, J. Alloys Compd. **825**, ID 154166 (2020). https://doi.org/10.1016/j.jallcom.2020.154166
16. B. S. Kalanoor, H. Seo, and S. S. Kalanur, Mater. Sci. Energy Technol. **1**, 49 (2018). https://doi.org/10.1016/j.mset.2018.03.004

17. D. Ni, J. Zhang, J. Wang, P. Hu, Y. Jin, Z. Tang, Z. Yao, W. Bu, and J. Shi, ACS Nano **11**, 4256 (2017). https://doi.org/10.1021/acsnano.7b01297
18. H. Q. Wang, P. F. Hu, Y. Zheng, Z. Zhao, B. Zheng, J. Chang, H. J. Wang, and J. H. Wang, Mater. Sci. Eng. C **80**, 102 (2017). https://doi.org/10.1016/j.msec.2017.05.131
19. F. Mehmood, J. Iqbal, T. Jan, and Q. Mansoor, Vib. Spectrosc. **93**, 78 (2017). https://doi.org/10.1016/j.vibspec.2017.09.005
20. C. Wang, Y. Gao, X. Gao, H. Wang, J. Tian, L. Wang, B. Zhou, Z. Ye, J. Wan, and W. Wen, Sci. Rep. **6**, ID 35876 (2016). https://doi.org/10.1038/srep35876
21. C. Guo, S. Yin, H. Yu, S. Liu, Q. Dong, T. Goto, Z. Zhang, Y. Li, and T. Sato, Nanoscale **5**, 6469 (2013). https://doi.org/10.1039/c3nr01025b
22. M. Selvamani, G. Krishnamoorthy, M. Ramadoss, P. K. Sivakumar, M. Settu, S. Ranganathan, and N. Vengidusamy, Mater. Sci. Eng. C **60**, 109 (2016). https://doi.org/10.1016/j.msec.2015.11.002
23. L. Wen, L. Chen, S. Zheng, J. Zeng, G. Duan, Y. Wang, G. Wang, Z. Chai, Z. Li, and M. Gao, Adv. Mater. **25**, 5072 (2016). https://doi.org/10.1002/adma.201506428
24. W. Guo, C. Guo, N. Zheng, T. Sun, and S. Liu, Adv. Mater. **29**, ID 1604157 (2016). https://doi.org/10.1002/adma.201604157
25. L. Wen, L. Chen, S. Zheng, J. Zeng, G. Duan, Y. Wang, G. Wang, Z. Chai, Z. Li, and M. Gao, Adv. Mater. **25**, 5072 (2016). https://doi.org/10.1002/adma.201506428
26. B. Manjunatha, A. N. Shetty, S. Kaveri, S. S. Mety, K. C. Anjaneya, R. Reddy, and S. Kalyane, Bionanoscience **10**, 73 (2019). https://doi.org/10.1007/s12668–019–00679-z
27. N. Kumara, B. P. A. George, B. P. A. H. Abrahamse, V. Parashar, and J. C. Ngila, Appl. Surface Sci. **396**, 8 (2016). https://doi.org/10.1016/j.apsusc.2016.11.027
28. MTT Cell Proliferation Assay Instruction Guide – ATCC, VA, USA www.atcc.org
29. D. Muhammad. D. M. M. Matin, S. M. R. Miah, and P. Devi, Electronic J. Chem. **13**, 250 (2021). https://doi.org/10.17807/orbital.v13i3.1614
30. H. Nazıra, M. M. Yıldızb, H.Yılmaz, M. N. Tahir, and D. Ulku, J. Molecul. Struct. **524**, 241 (2000). https://doi.org/10.1016/S0022–2860(00)00393–8
31. F. Mehmood, J. Iqbal, M. Ismail, and A. Mehmood, J. Alloys Compd. **746**, 729 (2018). https://doi.org/10.1016/j.jallcom.2018.01.409
32. F. Mehmood, J. Iqbal, T. Jan, W. Ahmed, W. Ahmed, A. Arshad, Q. Mansoor, S. Z. Ilyas, M. Ismail, and I. Ahmad, Ceram. Int. **42**, 14334 (2016). https://doi.org/10.1016/j.ceramint.2016.04.010
33. A. V. Viswanath, A. K. Gopinath, and C. S. Vijayamohanan, J. Appl. Phys. **100**, ID 074319 (2006). https://doi.org/10.1063/1.2356788
34. T. Aoki, T. Matsushita, A. Suzuki, K. Tanabe, and Okuda, J. Vacuum Sci. Technol. **23**, 1325 (2005). https://doi.org/10.1116/1.1978891
35. S. Brunauer, P. H. Emmett, and E. Teller, J. Am. Chem. Soc. **60**, 309 (1938). https://doi.org/10.1021/ja01269a023
36. M. Joshi, H. D. Juneja, and J. P. Kanfade, Int. J. Knowledge Eng. **3**, 69 (2012).
37. C. Martin, I. Martin, V. Rives, G. Solana, V. Loddo, L. Palmisano, and A. Sclafani, J. Mater. Sci. **32**, 6039 (1997). https://doi.org/10.1023/A:1018631531546
38. S. Supothina, S. seeharay, and P. Yoriya, Thailand Mater. Sci.Technol. 25 (1997).
39. S. V. Chong and J. l. Tallon, Indust. Res. Ltd , **67**, 235 (2018)
40. N. D. Hoa, N. V. Quy, Y. Cho, and K. Dojin, Sens. Actuators B **135**, 656 (2009). https://doi.org/10.1016/j.snb.2008.10.041
41. O. Rezaee, H. Mahmoudi Chenari, and F. E. Ghodsi, J. Sol-Gel Sci. Technol. 1 (2016).
42. S. A. El-Safty, A. Shahat, M. Mekawy, N. Hoa, W. Warkocki, and M. Ohnuma, Nanotechnology **21**, ID 375603 (2010). https://doi.org/10.1088/0957–4484/21/37/375603
43. S. Brunauer, P. H. Emmett, and E. Teller, J. Am. Chem. Soc. **60**, 309 (1938). https://doi.org/10.1021/ja01269a023
44. M. Joshi, H. D. Juneja, and J. P. Kanfade, Int. J. Knowledge Eng. **3**, 69 (2012).